

The CARMENES search for exoplanets around M dwarfs

The template division telluric modeling technique and its application to optical and near-infrared radial velocities

E. Nagel¹, S. Czesla¹, A. Kaminski², M. Zechmeister³, L. Tal-Or^{3,4}, J. H. M. M. Schmitt¹, I. Ribas^{5,6}, A. Reiners³, A. Quirrenbach², P. J. Amado⁷, J. A. Caballero⁸, J. M. Alacid⁸, F. F. Bauer⁷, V. J. S. Béjar⁹, M. Cortés-Contreras⁸, S. Dreizler³, A. Hatzes¹⁰, S. V. Jeffers³, M. Kürster¹¹, M. Lafarga^{5,6}, D. Montes¹², J. C. Morales^{5,6}, and S. Pedraz¹³

¹ Hamburger Sternwarte, Gojenbergsweg 112, 21029 Hamburg, Germany

e-mail: evangelos.nagel@hs.uni-hamburg.de

² Landessternwarte, Zentrum für Astronomie der Universität Heidelberg, Königstuhl 12, 69117 Heidelberg, Germany

³ Universität Göttingen, Institut für Astrophysik, Friedrich-Hund-Platz 1, 37077 Göttingen, Germany

⁴ Department of Geophysics, Raymond and Beverly Sackler Faculty of Exact Sciences, Tel Aviv University, Tel Aviv 6997801, Israel

⁵ Institut de Ciències de l'Espai (ICE, CSIC), Campus UAB, C/ de Can Magrans s/n, 08193 Cerdanyola del Vallès, Spain

⁶ Institut d'Estudis Espacials de Catalunya (IEEC), C/ Gran Capità 2-4, 08034 Barcelona, Spain

⁷ Instituto de Astrofísica de Andalucía (IAA-CSIC), Glorieta de la Astronomía s/n, 18008 Granada, Spain

⁸ Centro de Astrobiología (CSIC-INTA), ESAC, Camino Bajo del Castillo s/n, 28692 Villanueva de la Cañada, Madrid, Spain

⁹ Instituto de Astrofísica de Canarias, Vía Láctea s/n, 38205 La Laguna, Tenerife, Spain

¹⁰ Thüringer Landessternwarte Tautenburg, Sternwarte 5, 07778 Tautenburg, Germany

¹¹ Max-Planck-Institut für Astronomie, Königstuhl 17, 69117 Heidelberg, Germany

¹² Departamento de Física de la Tierra y Astrofísica and IPARCOS-UCM (Instituto de Física de Partículas y del Cosmos de la UCM), Facultad de Ciencias Físicas, Universidad Complutense de Madrid, E-28040, Madrid, Spain

¹³ Centro Astronómico Hispano-Alemán (CSIC-MPG), Observatorio Astronómico de Calar Alto, Sierra de los Filabres, 04550 Gérgal, Almería, Spain

Received date / Accepted date

ABSTRACT

Telluric contamination in ground-based optical and infrared spectroscopy is an important limiting factor in achieving maximum radial velocity (RV) precision with the aim of detecting Earth-like planets orbiting low-mass stars. Here we present the template division telluric modeling (TDTM) technique, a method to accurately remove telluric absorption lines in stars that exhibit numerous intrinsic features. Based on the Earth's barycentric motion through the year, our approach is suited to disentangle telluric and stellar spectral components. By fitting a synthetic transmission model, telluric-free spectra are subsequently derived. We demonstrate the performance of the TDTM technique in correcting telluric contamination using high-resolution optical and near-infrared spectral time series of the rapidly rotating A0-type star 109 Vir and the feature-rich M dwarfs GJ 273 (Luyten's star, M3.5 V) and GJ 1012 (M4.0 V) obtained with the CARMENES spectrograph. As GJ 1012 has been shown to show particularly low RV variability, we used its spectral time series to study the impact of our TDTM correction on the achievable RV precision. While the RV precision obtained in the optical arm is comparable to that produced by conservative masking of telluric features, we achieve a highly significant improvement in the near-infrared range. For GJ 1012 we find that the RV scatter decreases from 9.5 m s^{-1} to 5.7 m s^{-1} after applying the TDTM approach. Although the decrease in RV scatter is expectedly driven by the most heavily contaminated echelle orders close to strong telluric water bands, improvement is demonstrated over the entire wavelength range covered by the near-infrared channel of CARMENES. Our study emphasizes that the proper treatment of telluric lines in infrared high-precision RV studies is pivotal to push the capacity of near-infrared spectrographs to measure low-amplitude RV signals, and we demonstrate the power of our TDTM technique to achieve that.

Key words. atmospheric effects – instrumentation: spectrographs – methods: data analysis, observational – stars: low-mass – techniques: spectroscopic

1. Introduction

Ground-based spectroscopic observations at optical and near-infrared wavelengths are affected by absorption and emission features produced by the Earth's atmosphere. Rotational-vibrational transitions of molecules such as water (H_2O), oxygen (O_2), carbon dioxide (CO_2), and methane (CH_4) produce numerous absorption lines and broad absorption bands. Individual lines

vary in strength from shallow so-called micro-tellurics to strong lines with completely opaque line cores. These telluric lines are a common nuisance in ground-based spectroscopy.

The atmospheric conditions at the time of observation determine the telluric contribution to a stellar spectrum observed from the ground. The observed strength of the telluric lines depends on the location, in particular the elevation, of the observatory and the airmass of the target. Furthermore, telluric absorption lines

are Doppler shifted and broadened due to turbulent wind motions along the line of sight (e.g. Caccin et al. 1985). The atmospheric temperature and partial-pressure structure have a direct impact on the line profiles. The situation is further complicated by the temporal variability in temperature, pressure, and chemical composition of the Earth's atmosphere on seasonal, daily, and hourly time scales, which is particularly pronounced for the atmospheric water vapor content (Smette et al. 2015).

The detection of Earth-like rocky planets orbiting in the habitable zones of their host stars, requires very precise radial velocity (RV) measurements. In this context, the correction of telluric features has come into focus as one of the main contributors to the RV error budget (Halverson et al. 2016). Cool, low-mass M dwarfs are particularly promising targets for detecting rocky habitable-zone planets because of their relatively short orbital periods of around 20 d and the favorable planet-to-star mass ratios. As M dwarfs are intrinsically faint in the visible wavelength range and emit the bulk of their energy at $\sim 1\mu\text{m}$, a new generation of high-resolution spectrographs, such as CARMENES (Quirrenbach et al. 2018), NIRPS (Wildi et al. 2017), SPIRou (Donati et al. 2018), HPF (Mahadevan et al. 2014), and IRD (Kotani et al. 2018), have been designed and built to exploit the near-infrared wavelength range for RV planet searches. In this range, however, also telluric contamination is particularly severe. Reiners et al. (2018) showed that the highest RV precision for early and mid- M dwarfs can be reached in the wavelength range 700–900 nm. Wavelength ranges contaminated by telluric absorption were neglected in their analysis. Correction of this and other spectral regions that are heavily contaminated by O₂ and H₂O could significantly increase the RV precision in M dwarf observations.

A simplified approach to alleviate the impact of telluric lines on the RV measurement is to mask all telluric lines above a certain strength threshold prior to the RV computation. Indeed, this technique has been applied in many data-analysis pipelines devoted to extracting RVs from optical spectra, with satisfactory results (e.g., Anglada-Escudé & Butler 2012; Zechmeister et al. 2018). In the infrared, however, the ubiquity of telluric lines leads to extended masks. As a result, neglecting masked chunks of the stellar spectrum significantly limits our ability to study the infrared spectra and lowers the RV precision. Therefore, alternative techniques with better performance are called for.

To date, several elaborated approaches have been developed to correct for telluric lines, which can roughly be subdivided into empirical, data-driven, and forward-modeling approaches. A widely-used empirical technique is telluric division. Here telluric standard stars (TSSs) – usually rapidly rotating B- to A-type stars – are observed along with the science target observation, preferably similar in time, airmass, and direction as the science target. However, some compromises have to be made regarding these parameters. The drawbacks of the telluric division method have been extensively discussed, e.g., by Vacca et al. (2003), Bailey et al. (2007), Seifahrt et al. (2010), Gullikson et al. (2014), and Smette et al. (2015). Large RV surveys as those conducted by the HARPS and CARMENES collaborations refrain from frequent TSS observations because of the tremendous amount of additional observing time needed.

An empirical approach, avoiding frequent and repeated TSS observations, was presented by Artigau et al. (2014). These authors created a library of TSS spectra, observed on a dense grid of airmasses and water columns. By carrying out a principal component analysis, they identified independently varying spectral absorption patterns. Thus, telluric spectra were synthesized by using linear combinations of individual absorbances, which

Artigau et al. (2014) subsequently removed from HARPS measurements.

A data-driven technique involving machine-learning algorithms was presented by Bedell et al. (2019). Their `wobble` algorithm incorporates a model to simultaneously derive the stellar spectra, telluric spectra, and RVs from spectral time series without relying on external information on either the stellar or the telluric transmission spectrum.

While purely data-driven techniques are highly flexible, copious information on the atmosphere of the Earth and its spectrum is of course available. Synthetic transmission models of the spectrum of the Earth's atmosphere take advantage of this. They can be generated by radiative transfer codes (for an overview see Seifahrt et al. 2010) in combination with precise molecular line databases, and have become widely used (e.g., Bailey et al. 2007; Seifahrt et al. 2010; Lockwood et al. 2014; Husser & Ulrich 2014; Gullikson et al. 2014; Rudolf et al. 2016).

The software package `molecfit`¹, developed by Smette et al. (2015) and Kausch et al. (2015), implements a synthetic telluric transmission model and allows to correct observed spectra for telluric contamination. To that end, `molecfit` incorporates the line-by-line radiative transfer code LBLRTM (Clough et al. 2005) and the HITRAN molecular line list (Rothman et al. 2009). To synthesize a telluric spectrum, `molecfit` requires a number of parameters such as a model of the instrumental line spread function, an atmospheric profile describing the meteorological conditions during the observation, and the column density of the molecular species. In turn, the observed spectrum, which contains the telluric transmission spectrum, can be used to find best-fit values for these parameters. `Molecfit` does not consider the actual stellar spectrum, which occurs as a contaminant of the telluric spectrum in this context. Therefore, usually only a suitable subrange of the observed spectrum is used in the fit, which ideally contains moderately saturated telluric lines with a well-defined continuum. Based on the resulting atmospheric parameters, the telluric spectrum in the remaining range can then be inferred. While this approach works well in many cases, it becomes problematic in objects with ubiquitous intrinsic features such as M dwarfs, where the fitting becomes inaccurate because of numerous blends between stellar and telluric lines.

To address this problem, we present the template division telluric modeling (TDTM) technique. The heart of TDTM is the disentanglement of sections of the telluric and stellar spectrum by taking advantage of the relative shift between stellar and telluric lines caused by the Earth's barycentric motion. We then use `molecfit` to fit a synthetic transmission model to the extracted telluric spectrum and apply these results to correct for telluric absorption in the entire science spectrum. While the TDTM technique works independently of stellar spectral type, it is only applicable when spectroscopic time series sampling a range of barycentric velocity shifts are available.

Our paper is structured as follows. In Sect. 2 we describe the spectroscopic observations. The TDTM technique and the data preparation are presented in Sect. 3, and our findings are discussed in Sect. 4. Finally, we summarize our results in Sect. 5.

Table 1. Equatorial coordinates (J2000), G and J magnitudes, and number of used VIS and NIR spectra.

Name	α	δ	G^a [mag]	J^b [mag]	N_{VIS}	N_{NIR}
109 Vir	14 46 14.93	+01 53 34.39	3.6103 ± 0.0043	3.683 ± 0.244	163	154
GJ 273	07 27 24.50	+05 13 32.83	8.5945 ± 0.0003	5.714 ± 0.032	191	180
GJ 1012	00 28 39.47	-06 39 49.18	10.8947 ± 0.0007	8.038 ± 0.020	22	13

Notes. ^(a) Gaia Collaboration et al. (2018); ^(b) Cutri et al. (2003)

2. Observations and data reduction

The spectra used in this work were taken within the context of the CARMENES² survey. Constructed by eleven German and Spanish institutions, CARMENES consists of a pair of cross-dispersed fiber-fed échelle spectrographs, mounted on the 3.5 m telescope of the Calar Alto Observatory in Spain (Quirrenbach et al. 2018). CARMENES monitors the RVs of more than 300 M dwarfs to detect low-mass planets in their habitable zones (Reiners et al. 2018).

The instrument has two channels. The visual channel (VIS) provides wavelength coverage between 5 200 Å and 9 600 Å with a resolution of $R = 94\,600$, and the near-infrared channel (NIR) has a resolving power of $R = 80\,400$ and covers the spectral range from 9 600 Å to 17 100 Å. Both instruments are enclosed in vacuum vessels in the coudé room to ensure long-term stability. The data reduction was carried out using the standard CARMENES reduction pipeline CARACAL³ (Zechmeister et al. 2014; Caballero et al. 2016).

To demonstrate the performance and to evaluate the accuracy of the TDTM technique, we use observations of 109 Vir (HD 130109), an A0 V dwarf with $v \sin i = 285 \text{ km s}^{-1}$ (Royer et al. 2007), which is a regularly observed TSS in the CARMENES survey. In total, the time series consists of 163 VIS and 154 NIR observations taken between January 2017 and March 2019. In addition, we selected 191 VIS and 180 NIR observations of the bright M3.5 V dwarf GJ 273 (Luyten’s star) obtained between January 2016 and March 2019. GJ 273 serves as a typical representative of an object with a feature-rich spectrum. We demonstrate the improvement on the root-mean-square (rms) velocity dispersion achieved by the TDTM technique in the optical and near-infrared wavelength range using a sample of 22 VIS and 13 NIR spectra of the M4.0 V dwarf GJ 1012. This star was selected because it is a so-called RV-quiet star, characterized by weak RV variability with a standard deviation of only 2.2 m s^{-1} in the optical spectral range (Trifonov et al. 2018; Tal-Or et al. 2019). In Table 1 we provide information on the coordinates, G and J magnitudes, and on the number of used VIS and NIR spectra.

A typical signal-to-noise ratio (S/N) for CARMENES survey observations is 150 in the J band (Reiners et al. 2018), which translates into a median exposure time of 380 s for GJ 273 and 1800 s for GJ 1012. Since 109 Vir is a bright target ($J = 3.70$ mag), the typical exposure time of one minute already provides higher S/N.

¹ <http://www.eso.org/sci/software/pipelines/skytools/molecfit>

² Calar Alto high-Resolution search for M dwarfs with Exoearths with Near-infrared and optical Echelle Spectrographs.

³ CARMENES Reduction And CALibration

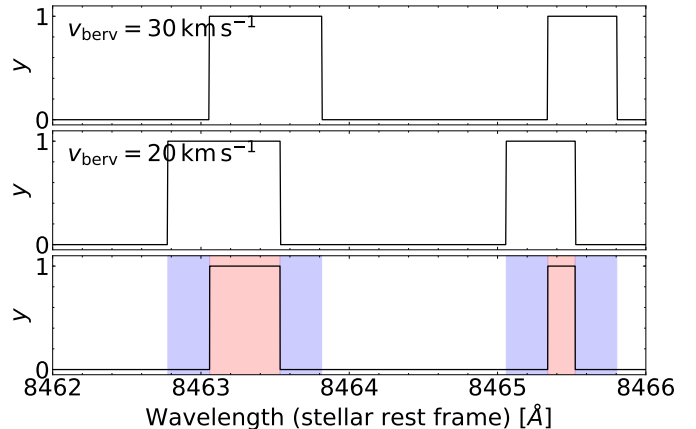


Fig. 1. *Upper and middle panels:* Small section of the telluric binary mask for two observations after the correction of the Earth’s barycentric motion. Wavelength ranges with $y = 1$ are masked as tellurics. *Lower panel:* Resulting mask of the template. Red shaded wavelength ranges correspond to template knots with $m_k = 0$ and contribute to the total masked template fraction γ . The blue shaded wavelength ranges are used for telluric modeling and contribute to γ' .

3. Correction method

Fitting telluric transmission models to observed M dwarf spectra is challenging because the stellar spectrum consists of numerous atomic and molecular lines without a true continuum. The fundamental idea behind the TDTM approach is to construct a high signal-to-noise template of the stellar spectrum from a spectral time series, which can be used subsequently to eliminate the stellar contribution and to model the residual telluric spectrum.

3.1. Template construction

We use the SERVAL⁴ code (Zechmeister et al. 2018) to compute the stellar template spectrum based on a time series of input spectra. Following the nomenclature of Zechmeister et al. (2018), we index the set of spectra by $n = 1, \dots, N$, and each spectrum is composed of flux density measurements $f_{n,i}$ at pixel i with uncertainties $\epsilon_{n,i}$ and calibrated wavelengths $\lambda_{n,i}$. We further write the observed spectrum in the form

$$f(\lambda_{n,i}) = [s(\lambda_{n,i}) \cdot t(\lambda_{n,i})] \otimes L(\lambda_i), \quad (1)$$

where $s(\lambda_{n,i})$ denotes the intrinsic stellar spectrum, $t(\lambda_{n,i})$ the telluric absorption spectrum at the time of observation, $L(\lambda_i)$ the line spread function, and \otimes the convolution operator.

In each observation, a stellar spectrum with a priori unknown RV shift and a telluric spectrum with variable properties, but

⁴ SpEcTrum Radial Velocity AnaLyser, <https://github.com/mzechmeister/serval>

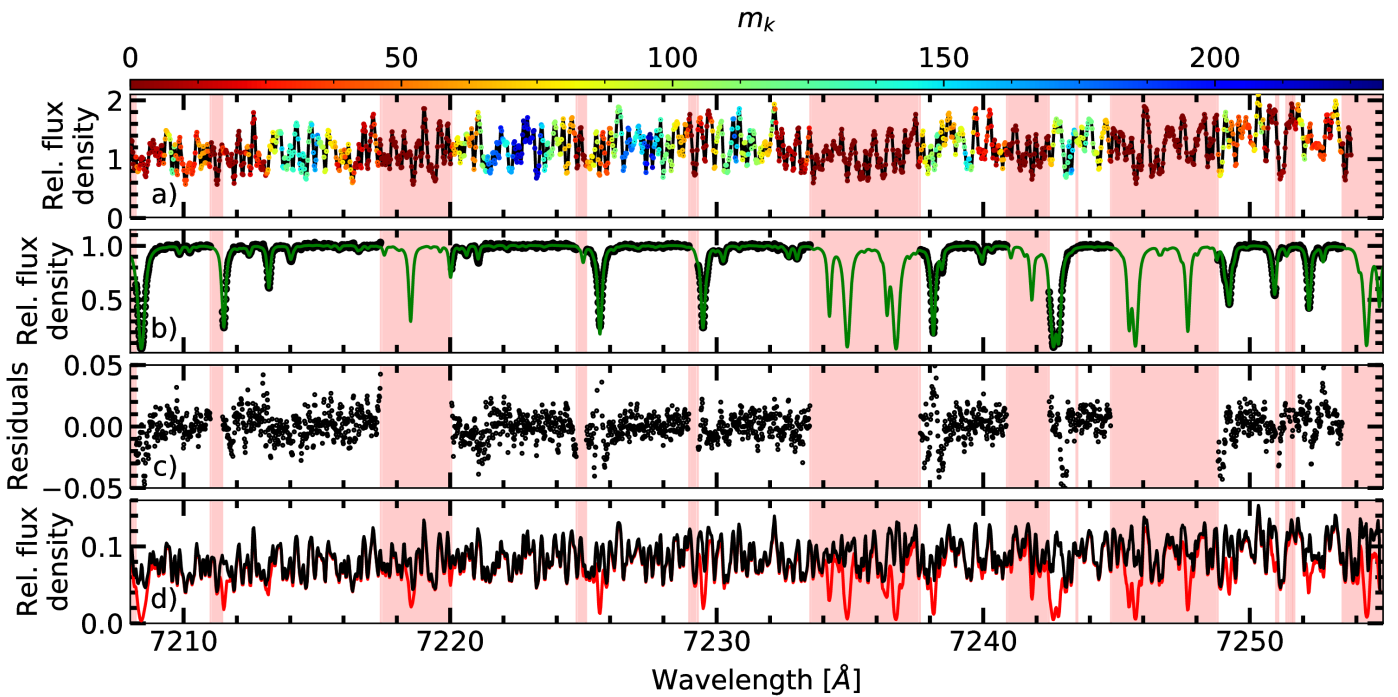


Fig. 2. Panel a: Segment of the optical template spectrum of GJ 273. Color-coded is the number m_k of exposure pixels that contribute to each template knot. The red shaded wavelength ranges mark knots with $m_k = 0$. Panel b: One residual telluric spectrum $f_{n,i}/s'(\lambda_i)$ (black dots) after the division of the science spectrum by the template, and best-fit telluric model ($T(\lambda_{n,i})$, green line) derived with molecfit. Red shaded wavelength ranges are excluded from the transmission model fit. Panel c: Absolute residuals $f_{n,i}/s'(\lambda_{n,i}) - T(\lambda_{n,i})$ of the fit. Panel d: CARMENES spectrum before ($f_{n,i}$, red line) and after ($f_{n,i}/T(\lambda_{n,i})$) correction with the transmission model derived with molecfit (black line).

fixed in the rest frame of the Earth, are superimposed. The ultimate goal of SERVAL is to derive precise measurements of the stellar RV. To that end, a preferably accurate and complete template of the stellar spectrum is required. This template is constructed by SERVAL from the spectral time series, following an iterative and sequential forward modeling approach.

Template completeness is improved by taking advantage of the relative RV shift of the stellar and telluric spectra induced by the Earth's barycentric motion, which can uncover sections of the stellar spectrum in some observations that may be affected by telluric lines in others with less favorable relative RV shift. To identify such sections, SERVAL uses a binary mask $m(\lambda_{n,i})$, flagging spectral pixels affected by known atmospheric absorption features that are typically deeper than 1 % (see Sect. 3.2). Additionally, SERVAL employs a bad-pixel map, which flags saturated pixels, outliers, pixels providing unphysical (negative) flux densities, and pixels affected by sky emission. Template S/N is improved by coadding the individual spectra after an appropriate RV shift. During this process, the spectra are transformed to the stellar rest frame, i.e. corrected for barycentric and stellar RVs. SERVAL also accounts for secular acceleration, a change in the stellar radial velocity due to the high proper motion of close-by stars (Kürster et al. 2003; Zechmeister et al. 2009).

As a starting point for RV and template calculation, SERVAL calculates preliminary RVs using the highest S/N spectrum of the CARMENES spectral time series as a template. These are subsequently used to improve the stellar template spectrum by coadding the individual spectra and obtain higher precision RVs. This process is repeated until convergence is achieved. All masked pixels are excluded and telluric affected heavily down-weighted in the process of coadding to isolate the stellar spectrum in the template.

The process of improving the template completeness by taking advantage of the relative shift of the mask is demonstrated in Fig. 1. The upper and middle panels show a segment of the telluric mask position of two observations after the correction for the Earth's barycentric motion. The lower panel shows the resulting mask of the template, assuming that the intrinsic RV shift of the stellar spectrum remained small. In the blue shaded regions, the stellar spectrum is seen in one of the observations, and only the red shaded ranges remain hidden. This results in an improvement of the template wavelength coverage.

Shifting the spectra to the same reference wavelength results in a wavelength sampling that differs for data taken at different nights. SERVAL avoids interpolating the spectra on a new discrete wavelength grid. Instead, a uniform cubic B-spline regression with knots k on a regular logarithmic wavelength $\ln \lambda_k$ grid is carried out. In essence, the template knots specify the wavelength grid of the template. Typically, the number of template knots is comparable to the number of pixels per spectral order. In the following, $s'_k(\lambda_k)$ refers to the stellar template flux density. As an example, a section of the template of GJ 273 is shown in Fig. 2a.

As a crucial quantity for the TDTM approach, we define m_k as the number of unflagged pixels that contribute to a knot. m_k is stored for each template knot. The link between m_k and the mask can be inferred from the lower panel of Fig. 1. In this specific example with only two observations, $m_k = 0$ for template knots falling into the red marked wavelength range, $m_k = 1$ for knots within the blue wavelength range, and $m_k = 2$ for the remaining part of the spectrum.

Therefore, given one particular template knot k , three situations are possible: (1) all pixels contributing to this knot contain spectral information (i.e., are not masked), (2) all pixels are

masked, (3) some pixels contain spectral information, while the remaining pixels are masked. The quantity m_k is maximized in case (1), decreases for knots partly affected by tellurics in case (3), and takes a value of $m_k = 0$ for pixels subject to case (2). For sampling reasons, spectra can contribute more than one pixel to a template knot, so that m_k can exceed the number N of observations. This is demonstrated in Fig. 2a, where a few template knots have $m_k \gtrsim 200$, although the number of observations is $N_{\text{VIS}} = 191$. The red shaded areas show wavelength ranges for which m_k is zero, i.e., the stellar spectrum could not be recovered.

As the total masked template fraction γ we define the fraction of masked ranges ($m_k = 0$) compared to the entire wavelength range of the spectrum. As a result, the template completeness corresponds to $1 - \gamma$ and will depend on berycentric RV of the observer. The wavelength ranges of the stellar spectrum characterized by overlapping masked and non-masked regions, indicated by the blue shaded areas in Fig. 1 and recovered in the process, are now additionally available for RV calculation and telluric modeling. We denote the total fraction of these ranges compared to the entire wavelength range of the spectrum by γ' .

3.2. Mask construction

The telluric mask is an essential ingredient of the TDTM technique. As telluric features are ubiquitous, mask construction needs to balance strictness and achievable template completeness. While a restrictive mask, covering all relevant telluric features, is crucial to create a useful stellar template, an overly strict mask, declaring extended chunks of the spectrum unusable, jeopardizes the derivation of a template with any practical value.

To construct masks, we computed a synthetic telluric transmission model including H_2O , O_2 , CO_2 , and CH_4 using `molecfit`. As input parameters we used the median observational and atmospheric parameters of the GJ 273 data set, and adopted the values from the standard atmosphere profile for the column densities of the atmospheric constituents. In the resulting transmission model, we normalized wavelength ranges affected by molecular continuum absorption. Finally, we computed a binary mask by flagging all model features deeper than a specified threshold. In our analysis, we found that a threshold of 1 % provides a reasonable compromise between capturing the vast majority of telluric features and removing critical amounts of usable spectrum.

3.3. Telluric spectrum extraction

To extract the telluric transmission spectrum, we need to remove the stellar contribution from the individual observations. Therefore, we appropriately shifted the template spectrum and followed Vacca et al. (2003) in approximating Eq. (1)⁵ by

$$f(\lambda_{n,i}) \approx [s(\lambda_{n,i}) \otimes L(\lambda_i)] \cdot [t(\lambda_{n,i}) \otimes L(\lambda_i)]. \quad (2)$$

Substituting the convolved intrinsic stellar flux density $s(\lambda_{n,i}) \otimes L(\lambda_i)$ by the template $s'(\lambda_i)$ we obtain

$$f(\lambda_{n,i}) \approx s'(\lambda_i) \cdot [t(\lambda_{n,i}) \otimes L(\lambda_i)]. \quad (3)$$

Dividing the observed spectra by the appropriately shifted template, we derive a residual spectrum that is essentially free of

Table 2. `Molecfit` fitting ranges used to calibrate the model for CARMENES VIS and NIR spectra.

Channel	$\Delta\lambda [\text{\AA}]$	Main absorber
VIS	6270 – 6324	O_2
VIS	6913 – 7070	$\text{O}_2, \text{H}_2\text{O}$
VIS	7148 – 7415	H_2O
VIS	7676 – 7714	O_2
VIS	7850 – 8425	H_2O
VIS	8890 – 9270	H_2O
NIR	9750 – 10 350	H_2O
NIR	10 600 – 11 000	H_2O
NIR	11 600 – 12 400	H_2O
NIR	12 400 – 13 100	O_2
NIR	15 110 – 15 400	H_2O
NIR	15 600 – 15 800	CO_2
NIR	15 900 – 16 200	CO_2
NIR	16 350 – 16 660	CH_4
NIR	16 850 – 17 100	$\text{CH}_4, \text{H}_2\text{O}$

stellar features

$$\frac{f(\lambda_{n,i})}{s'(\lambda_i)} \approx t(\lambda_{n,i}) \otimes L(\lambda_i). \quad (4)$$

As the uncertainty of the template is typically negligible compared to that of the individual observations as $m_k \gg 1$, we do not propagate the template uncertainty and use the uncertainty of the observed spectra in the modeling of the individual residual spectra.

The residual telluric transmission spectrum of GJ 273 is shown in Fig. 2b. Again, the red bands represent template knots for which the residual spectrum could not be constrained. Consequently, these sections are not used to model the telluric lines.

3.4. Telluric line modeling

The modeling of the residual telluric spectrum was performed using the `molecfit` package in version 1.5.9 (Smette et al. 2015; Kausch et al. 2015) and the molecular line list `aer`⁶ in version 3.6. The altitude stratification of temperature, pressure, and molecular abundances serves as input for LBLRTM. To create this profile, `molecfit` merges information from three sources: (1) a reference atmospheric profile, (2) Global Data Assimilation System (GDAS) profiles⁷, and (3) measurements of the ambient conditions obtained during the time of observations. In this study, we used a nightly mid-latitude (45°) reference model atmosphere⁸ as reference profile. Beside the pressure and temperature distribution up to an altitude of 120 km as function of height on a 1 km grid, the profile also provides the abundances of 30 molecules. The GDAS profiles describe the pressure, temperature, and relative humidity as a function of 23 altitude levels up to roughly 26 km.

In the spectral modeling with `molecfit`, we let the abundances of O_2 , CO_2 , CH_4 , and the atmospheric water vapor content vary freely. We carried out the model fitting over broad wavelength ranges that cover large portions of the molecular bands taking full advantage of numerous unsaturated telluric lines contained in the CARMENES optical and near-infrared

⁶ <http://rtweb.aer.com/>

⁷ <https://www.ready.noaa.gov/gdas1.php>

⁸ <http://eodg.atm.ox.ac.uk/RFM/atm/>

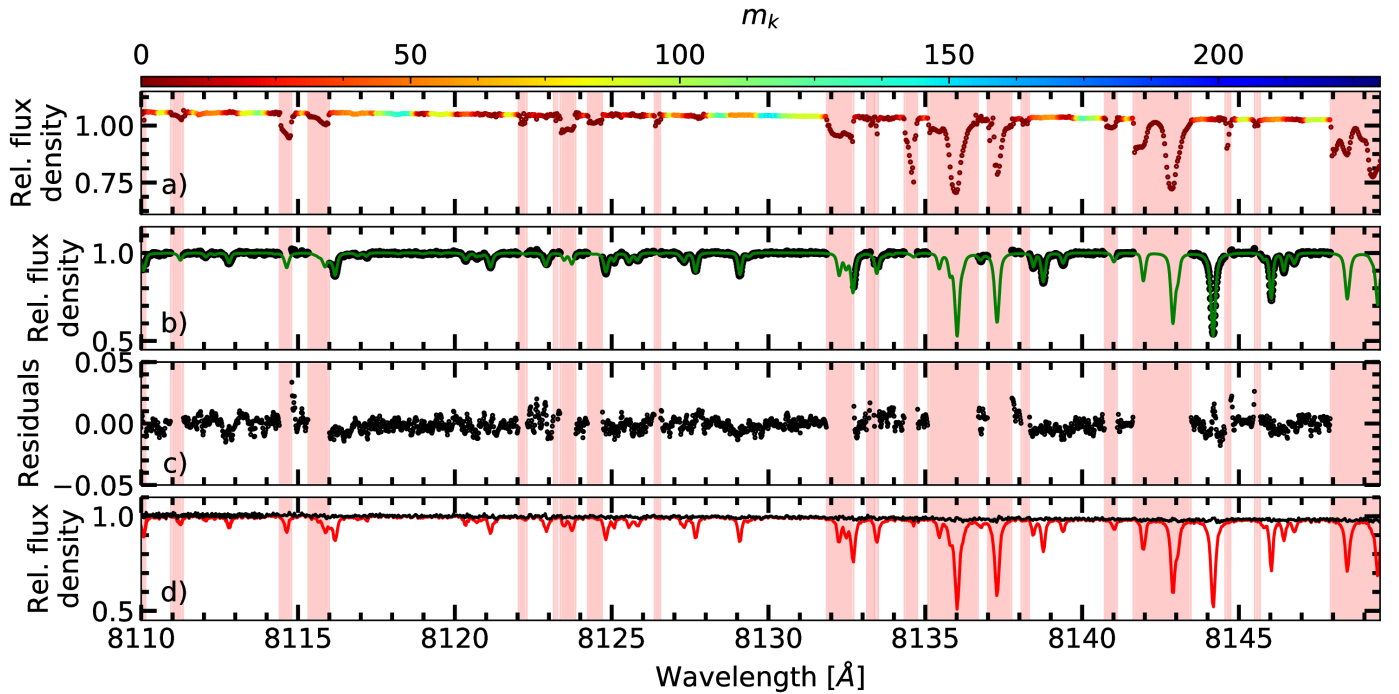


Fig. 3. Same as Fig. 2 but for the telluric standard star 109 Vir.

channel; the selected fitting intervals are given in Table 2. In the modeling, the continuum level within the fitting ranges was approximated with a low order polynomial. Since small errors in the wavelength calibration result in large residuals in the corrected spectra, we also allowed a Doppler shift of the transmission model to match the observed spectrum. In this way, instrumental drifts can be accounted for in the modeling. Wavelength ranges for which no stellar template was available ($m_k = 0$) were excluded from the fit along with sections affected by sky emission features.

Molecfit requires the instrumental line spread function in the modeling. In the case of CARMENES, this can be represented by a combination of two profiles, one Gaussian and one Lorentzian profile. We performed an extensive analysis to derive appropriate parameters for the line spread functions in both CARMENES channels based on calibration data (see Appendix A). Therefore, the parameters of the line spread function are not free in the modeling.

3.5. Telluric line removal

Having fitted a transmission model to the residual telluric spectrum with **molecfit**, we used the best-fit parameters as input to compute a synthetic transmission model over the entire wavelength range of the observation with the `calctrans` module of **molecfit**. To derive the spectrum corrected for telluric lines $F_{n,i}$, we finally divide the CARMENES observation by the transmission model $T(\lambda_{n,i})$

$$F_{n,i} = \frac{f_{n,i}}{T(\lambda_{n,i})}. \quad (5)$$

As an example, we show the observed and the telluric corrected spectrum of GJ 273 in Fig. 2d.

4. Results and discussion

4.1. Correction accuracy

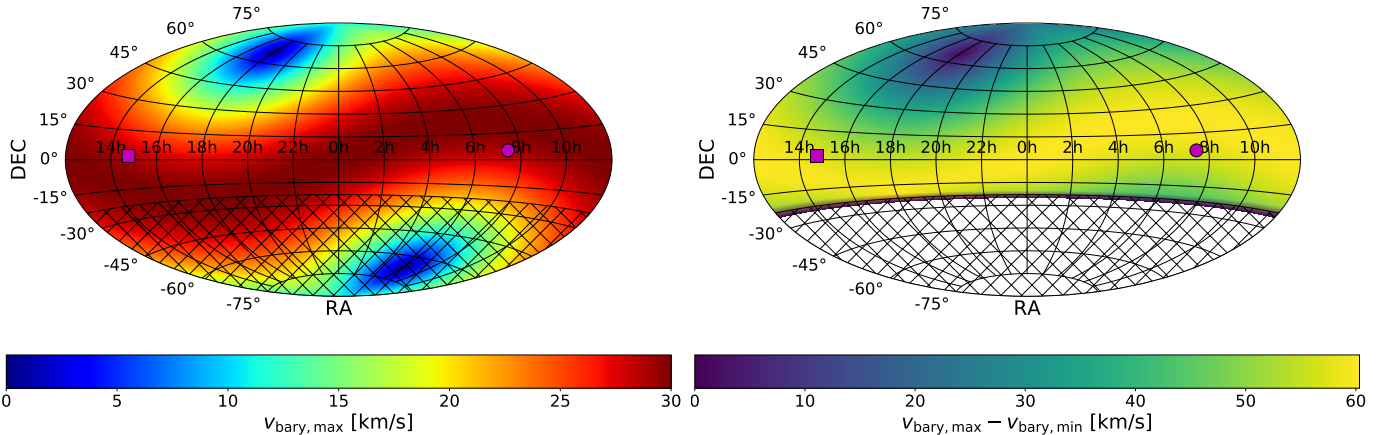
To demonstrate the use and evaluate the performance of the TDTM approach, we applied it to optical and near-infrared CARMENES observations of the TSS 109 Vir and the M dwarf GJ 273. We present an example of the correction procedure for 109 Vir in Fig. 3. Panel a) shows the template spectrum, which is free of stellar lines. Wavelength ranges where m_k is zero are heavily affected by tellurics. The template is noisier in wavelength ranges where m_k small (e.g. at 8121 Å). To obtain a more robust template, the m_k limit can be increased.

The correction accuracy strongly depends on the S/N of the data and the depth of the telluric features. As shown in Fig. 3d, micro-tellurics and lines with up to $\sim 50\%$ depth can be corrected basically to within the noise level. Deeper lines are problematic for two reasons. First, the S/N decreases in their cores and, second, lines deeper than 50 % leave comparatively large systematic residuals in the corrected spectra especially in the line cores. These residuals may be attributed to the fact that small discrepancies between model and observation can result in large residuals, especially in deep lines. These discrepancies may result from uncertainties of the line strengths listed in the HITRAN database, leading to inaccurate column density fits (Seifahrt et al. 2010; Gordon et al. 2011). Potential uncertainties in the line positions affect the wavelength calibration causing P Cygni-like residuals in the worst cases. Incomplete corrections may also arise from the instrumental line profile model. In fact, the Gaussian and Lorentzian profile parameters from different lines show some scatter and are approximated by a constant value (see Appendix A). Another source of uncertainty is the approximation of Eq. (1) by Eq. (2), which becomes particularly relevant in the case of blends between telluric and stellar lines (Sameshima et al. 2018, Appendix B).

To evaluate the accuracy of the telluric removal we identified wavelength ranges in the spectrum of 109 Vir that do not contain

Table 3. Individual wavelength ranges of O₂, H₂O, and CO₂ bands used to assess the quality of the telluric correction in spectra of 109 Vir.

Species	Telluric corrected			Reference		
	λ_{\min} [Å]	λ_{\max} [Å]	$\bar{\sigma}$ [%]	λ_{\min} [Å]	λ_{\max} [Å]	$\bar{\sigma}$ [%]
O ₂	6277	6323	1.1	6265	6275	0.6
O ₂	6924	6964	0.5	6850	6865	0.7
H ₂ O	7258	7325	0.6	7440	7480	0.5
O ₂	7676	7715	0.8	7720	7755	0.5
H ₂ O	8219	8247	1.1	8247	8254	0.5
H ₂ O	9810	9856	0.9	9880	9910	0.6
O ₂	12490	12576	1.0	12440	12460	0.6
CO ₂	15990	16023	1.1	15930	15970	1.0

**Fig. 4.** Sky maps in Aitoff projection of the maximum absolute barycentric RV $v_{\text{bary}, \text{max}}$ as derived from Eq.(8) (left panel) and full amplitude of the barycentric RV $v_{\text{bary}, \text{max}} - v_{\text{bary}, \text{min}}$ (right panel) for nights when the star is observable above 30° over the horizon for the location of the Calar Alto Observatory. Marked are the positions of 109 Vir (purple square) and GJ 273 (purple circle). The hatching pattern indicates the visibility cut-off at $\delta < -23^\circ$ of the CARMENES GTO survey.

stellar features but are contaminated with telluric lines of different strengths attributable to one molecular species. For each of these ranges, we defined a nearby wavelength region with similar S/N, which is basically free of telluric lines to serve as a reference. After we applied our correction, we continuum-normalized those wavelength intervals and computed the standard deviation of the spectral bins σ . The results for several telluric bands are presented in Table 3. Our analysis confirms that unsaturated telluric absorption features are corrected to within 2 % or better of the continuum standard deviation as reported by Smette et al. (2015). For objects with numerous intrinsic features, the authors proposed to apply `molecfit` to TSSs observations taken with the same instrumental setup as the science object, to solve for the polynomial continuum coefficients, and use the results as fixed input to subsequently apply `molecfit` to the science observation and to carry out the telluric correction. Our approach, however, is able to accurately and directly extract telluric features of various strengths for wavelength ranges with $m_k > 0$, even for feature-rich objects like M dwarfs, whose spectra are dominated by numerous molecular features in the optical and near-infrared bands.

For GJ 273 we show further examples of telluric contaminated wavelength ranges containing molecular bands of O₂, H₂O, and CO₂ in the Appendix (Figs. C.1 and C.2). Notably, molecular bands with an evenly spaced line structure such as the CO₂ band at $\sim 1.6\,\mu\text{m}$ can be almost fully restored (Fig. C.2).

4.2. Visibility constraints

For the TDTM technique to work properly, a good template is essential. While a lack of S/N may be addressed by taking more observations, which may pose a practical but not a fundamental problem, the relative shift between telluric and stellar lines is also crucial for the template construction. In the case of planet-induced reflex motion, the barycentric motion of the Earth and its rotation dominate the sum of relative shifts. The maximum absolute barycentric velocity $v_{\text{bary}, \text{max}}$ depends on the ecliptic latitude β of a target

$$v_{\text{bary}, \text{max}} \approx 30 \text{ km s}^{-1} |\cos \beta|. \quad (6)$$

The transformation from the equatorial (λ, β) to the ecliptic system (α, δ) with the inclination of the Earth $\varepsilon \approx 23^\circ$ yields

$$\sin \beta = \sin \delta \cos \varepsilon - \cos \delta \sin \alpha \sin \varepsilon. \quad (7)$$

Thus $v_{\text{bary}, \text{max}}$ as a function of α and δ reads

$$v_{\text{bary}, \text{max}}(\alpha, \delta) \approx 30 \text{ km s}^{-1} \sqrt{1 - \sin^2 \beta(\alpha, \delta)}, \quad (8)$$

which provides a sky map as in the left panel of Fig. 4 showing the maximum offset between telluric lines and stellar lines. Except for objects situated near the ecliptic poles, $v_{\text{bary}, \text{max}}$ is larger than the natural line width of the tellurics and the instrumental resolution ($\sim 3 \text{ km s}^{-1}$), which is required to disentangle the stellar and telluric spectra.

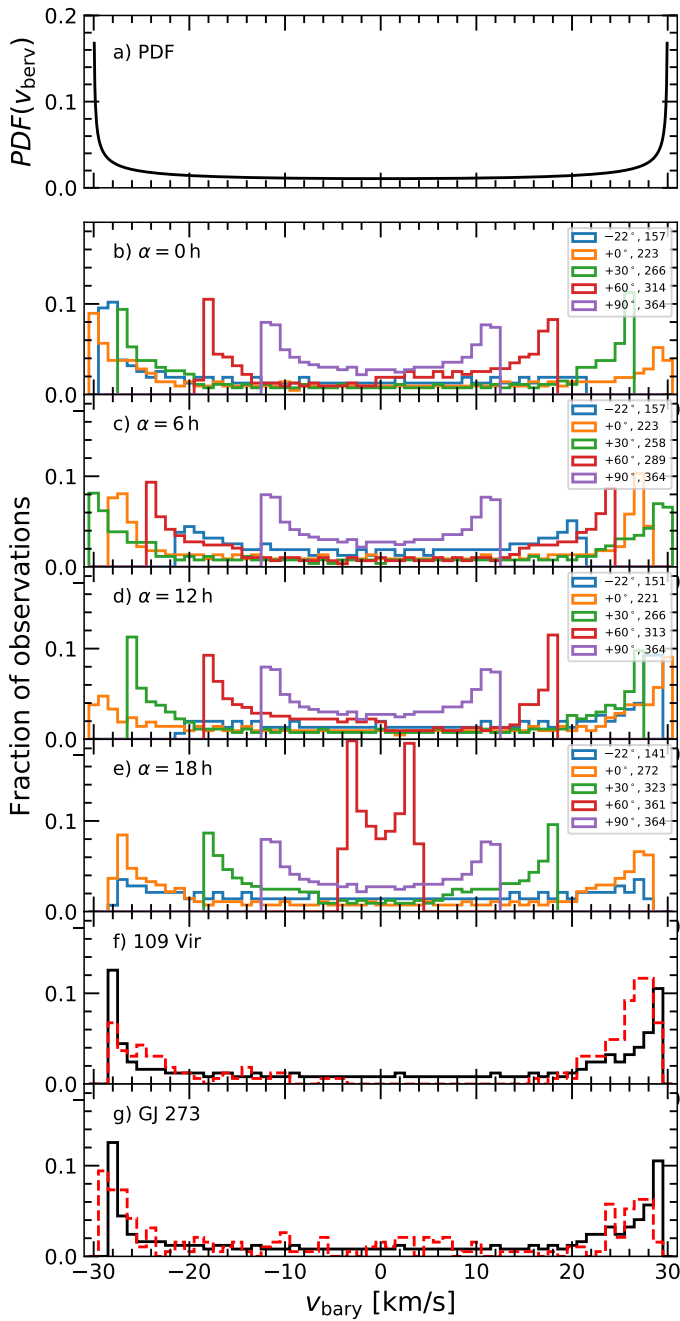


Fig. 5. Panel *a*: Probability density function $PDF(v_{\text{bary}})$ as computed with Eq.(11). Panels *b-e*: Simulated barycentric velocity distributions for targets with $\alpha = 0\text{h}, 6\text{h}, 12\text{h}$, and 18h , and $\delta = -22^\circ, 0^\circ, +30^\circ, +60^\circ, +90^\circ$, assuming one daily measurement over a time span of one year and considering the target visibility. The second entry in the legend is the number of total observing nights. Panels *f-g*: Simulated barycentric velocity distribution of 109 Vir and GJ 273 (black lines). Overplotted are the barycentric velocity distributions for the datasets of 109 Vir and GJ 273 (red dashed lines).

To examine the largest possible improvement on the template completeness, we carried out a simulation of the full amplitude of the barycentric velocity range $v_{\text{bary, max}} - v_{\text{bary, min}}$ as a function of ecliptic coordinates down to the visibility cut-off for stars with $\delta < 23^\circ$, which is also the CARMENES GTO survey limit (Garcia-Piquer et al. 2017). In particular, we computed the dates

on which a target is 30° above the horizon between the astronomical dusk and dawn for the location of the Calar Alto Observatory and calculated the barycentric RV at midnight for those dates. In the right panel of Fig. 4 we show the difference between the maximum and minimum barycentric RV $v_{\text{bary, max}} - v_{\text{bary, min}}$ for each pair of coordinates.

The observed barycentric velocity range is further constrained by the visibility. The main contribution to the barycentric velocity is a yearly sinusoid. We consider an object with a half-year visibility period, during which the barycentric Earth RV changes from a maximum to a minimum. In particular, we can consider the first half of a cosine

$$v_{\text{bary}}(t) = v_{\text{bary, max}} \cdot \cos\left(\frac{2\pi t}{T_\oplus}\right), \quad (9)$$

where T_\oplus is the orbital period of the Earth. When the target is observed at a random time, the probability to observe a barycentric RV shift equal or smaller than v_{obs} is

$$P(v_{\text{bary}} \leq v_{\text{obs}}) = 1 - \frac{1}{\pi} \arccos\left(\frac{v_{\text{obs}}}{v_{\text{bary, max}}}\right). \quad (10)$$

The probability density function ($PDF(v_{\text{bary}})$) to observe the target in some interval of barycentric velocity is given by

$$PDF(v_{\text{bary}}) = \frac{1}{\pi v_{\text{bary, max}} \sqrt{1 - \left(\frac{v_{\text{bary}}}{v_{\text{bary, max}}}\right)^2}}, \quad (11)$$

which is shown in Fig. 5a.

To study the barycentric velocity distribution as a function of right ascension and declination over one year for the location of the Calar Alto Observatory, we carried out simulations for a set of coordinates with $\alpha = 0\text{h}, 6\text{h}, 12\text{h}$, and 18h , and $\delta = 0^\circ, +30^\circ, +60^\circ$, and $+90^\circ$. In addition, we included a southern coordinate sample with $\delta = -22^\circ$, which is near the visibility limit of the CARMENES survey. Assuming that objects can generally only be observed down to an elevation of 30° , we determined the nights when the target is observable and computed the barycentric velocity at the time between evening and morning astronomical twilight. Our results are presented in Fig. 5b-e. The simulated distributions show a flat plateau around $v_{\text{bary}} = 0$ and increase at both ends where $v_{\text{bary}} \rightarrow \pm v_{\text{bary, max}}$. This shape is a consequence of the regular sampling of the yearly sinusoidal barycentric velocity contribution. However, the simulations show that all barycentric velocities between $-v_{\text{bary, max}}$ and $+v_{\text{bary, max}}$ are covered. We finally present the predicted and observed barycentric velocity distributions of 109 Vir (Fig. 5f) and GJ 273 (Fig. 5g) of our spectroscopic data sets.

4.3. Total masking fraction

A mask that flags telluric features deeper than 1% results in a total masking fraction $\gamma_{\text{max, VIS}} = 33.6\%$ for the optical spectral range ($0.52\text{--}0.96\mu\text{m}$) and $\gamma_{\text{max, NIR}} = 59.1\%$ for the near-infrared ($0.96\text{--}1.71\mu\text{m}$). For the default 5% mask provided by SERVAL we derive total masking fractions of $\gamma_{\text{max, VIS}} = 14.6\%$ and $\gamma_{\text{max, NIR}} = 37.1\%$. As the number of observations with different barycentric velocities is increased, the total masked fraction decreases and converges to a limit of $\gamma_{\text{min, VIS}} = 17.1\%$ and $\gamma_{\text{min, NIR}} = 39.1\%$ for the 1% mask, and $\gamma_{\text{min, VIS}} = 5.2\%$ and $\gamma_{\text{min, NIR}} = 19.8\%$ for the 5% default mask from SERVAL. These limits are mainly defined by broad telluric features, e.g.

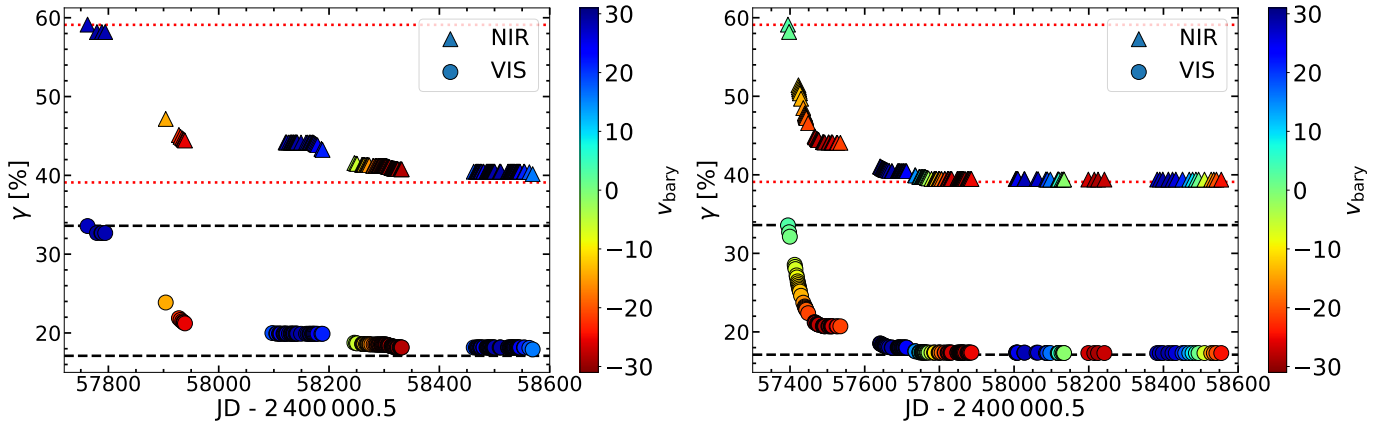


Fig. 6. Evolution of the total masked wavelength fraction color-coded with the barycentric velocity for 109 Vir (left) and GJ 273 (right). The circles represent the VIS channel and the triangles the NIR channel. The upper and lower dashed black lines mark the maximum and minimum limits of the total masked fraction in the optical wavelength range. The dotted red lines mark the same limits for the near-infrared wavelength range.

the strong water bands centered around $1.15 \mu\text{m}$ and $1.4 \mu\text{m}$, which prevent further reduction of masked regions.

The difference between the maximum and minimum masking fraction is the total fraction that is gained for the modeling of the telluric spectrum, which is $\gamma'_{\max, \text{VIS}} = 16.5\%$ in the optical and $\gamma'_{\max, \text{NIR}} = 20.0\%$ in the near-infrared employing the 1 % mask, and $\gamma'_{\max, \text{VIS}} = 9.4\%$ and $\gamma'_{\max, \text{NIR}} = 17.3\%$ for the default 5 % mask. In the VIS, the useable amount of the stellar spectrum was increased from 66.4 % to 82.9 %, which corresponds to a growth of 24.9 % for the 1 % mask. The increment is even larger in the NIR, where we find that the useable range was increased from 40.9 % to 60.9 %, which corresponds to a growth of 48.9 %. For the 5 % mask we extend the usable range from 85.4 % to 94.8 % by 11.0 % in the VIS and from 62.9 % to 80.2 % by 27.5 % in the NIR.

We show the evolution of the total masked fraction using the 1 % mask for 109 Vir and GJ 273 in Fig. 6. To reach the lower limit of the total masked fraction it is necessary to cover the full range of barycentric velocities. As shown in Fig. 6, this requirement was fulfilled for GJ 273 after the first observing season. In the case of 109 Vir, the lack of observations with barycentric velocities between $-3 \text{ km s}^{-1} < v_{\text{berv}} < 15 \text{ km s}^{-1}$ (see Fig. 5) prevented reaching the lower limit of the total masked fraction. However, as shown in Fig. 6, only a few observations at $\sim \pm 30 \text{ km s}^{-1}$ are required to substantially decrease the total masked fraction. Moreover, we found in our simulations that six observations equally distributed in the barycentric velocity space of $\pm 30 \text{ km s}^{-1}$ are sufficient to reach a value of 17.9 % in VIS and 40.3 % in NIR.

4.4. Impact on RV measurements

To study the impact of the telluric correction on the RV precision in the wavelength range covered by the VIS and NIR channel of CARMENES, we applied our method to 22 VIS and 13 NIR observations of the RV-quiet star GJ 1012. We then derived RVs using both the original spectra and those corrected for telluric absorption. Using spectra without any telluric correction, we derived RVs employing the default 5 % telluric mask provided by SERVAL (Zechmeister et al. 2018). To take advantage of the more extended wavelength range accessible after telluric correction, we followed the procedure described in Sect. 3.2 to

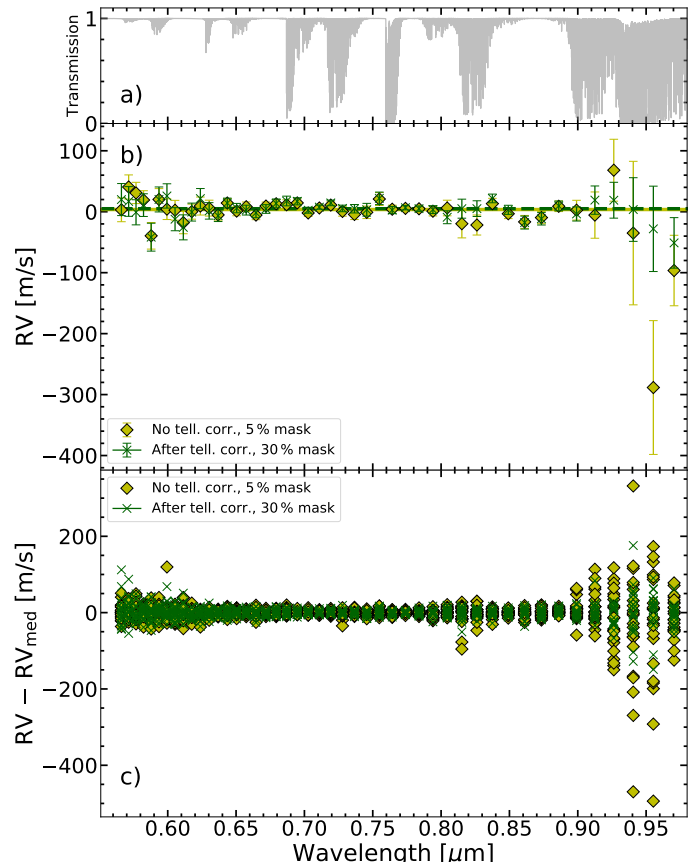


Fig. 7. Panel a: Synthetic transmission spectrum covering the wavelength range of the CARMENES VIS channel. Panel b: Radial velocities measured in 46 spectral orders before (yellow diamonds) and after telluric correction (green crosses) of one CARMENES VIS observation of GJ 1012. The horizontal lines indicate the median RVs before (solid yellow) and after telluric correction (dashed green). Panel c: Difference between measured and median RVs calculated in 46 spectral orders before (yellow diamonds) and after telluric correction (green crosses) using 22 CARMENES VIS observations of GJ 1012.

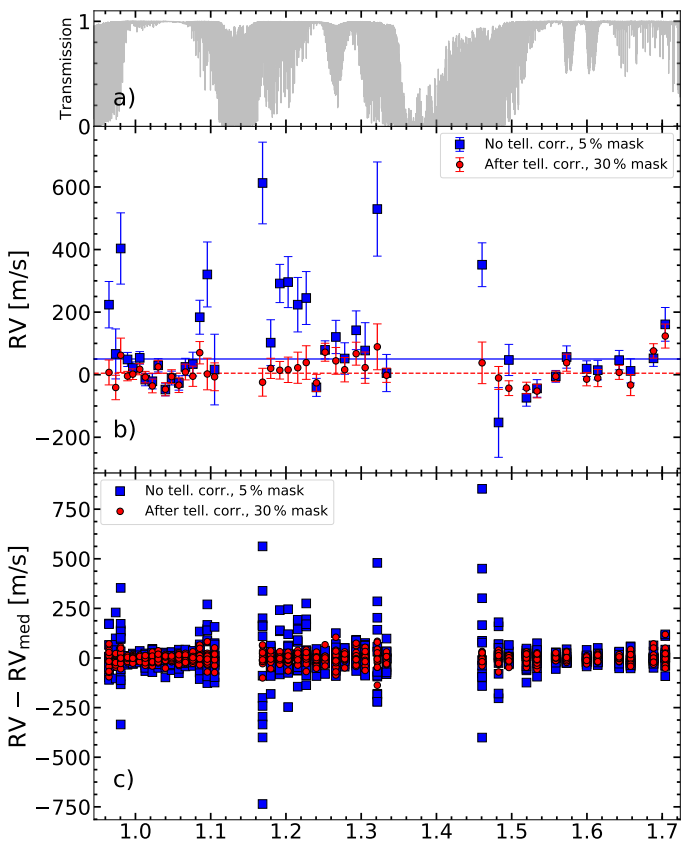


Fig. 8. Panel a: Synthetic transmission spectrum covering the wavelength range of the CARMENES NIR channel. Panel b: Radial velocities measured in 44 spectral orders before (blue squares) and after telluric correction (red circles) of one CARMENES NIR observation of GJ 1012. The horizontal lines indicate the median RVs before (solid blue) and after telluric correction (dashed red). Panel c: Difference between measured and median RVs calculated in 44 spectral orders before (blue squares) and after telluric correction (red circles) using 13 CARMENES NIR observations of GJ 1012.

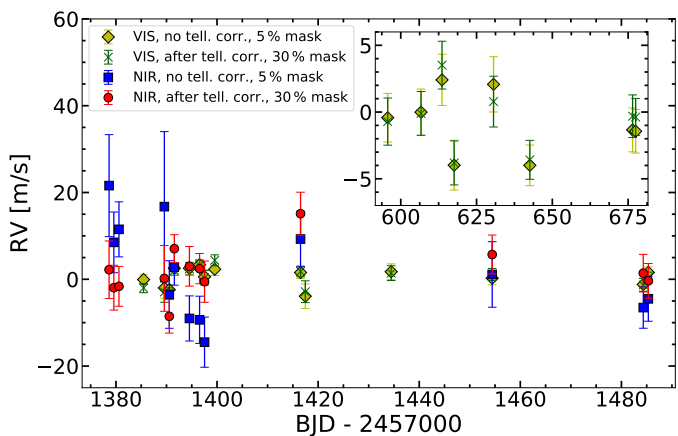


Fig. 9. Radial velocity measurements before (VIS: yellow diamonds; NIR: blue squares) and after (VIS: green crosses; NIR: red circles) the telluric correction as a function of barycentric Julian Date for GJ 1012 obtained with the VIS and NIR channel of CARMENES. The first eight VIS RVs are shown in the inset for the sake of clarity.

construct a less conservative telluric mask, excluding only spectral regions, which are affected by atmospheric transmission features deeper than 30 %. We used this mask to determine RVs from telluric corrected observations.

We show the RV measurements before and after the telluric correction per spectral order exemplarily for one single VIS and NIR spectrum in Fig. 7b and Fig. 8b, respectively. The weighted medians over the RVs computed over all orders are indicated by the horizontal lines. In addition, a synthetic atmospheric transmission spectrum is plotted in Fig. 7a and Fig. 8a to illustrate the location of the telluric absorption bands. The largest impact of the telluric correction obviously occurs in orders that are strongly affected by telluric absorption. In the VIS range we found a lower RV dispersion in orders covering the water bands from 0.90 to 0.97 μm . A less pronounced improvement was found for orders that are affected by the water band located between 0.80 and 0.85 μm . The wavelength range at 0.56–0.62 μm , however, shows a somewhat odd behavior. Although this range is covered by rather shallow telluric features, the telluric correction causes a slight increase of the RV scatter. A visual inspection of these orders did not reveal indications for an inaccurate telluric correction. Despite a thorough examination with regard to our procedure and the RV determination, the reason remains unclear. For the NIR channel we found that RVs determined in orders close to the nearly opaque water bands centered at about 0.95, 1.14, and 1.40 μm differ by up to several hundreds of m s^{-1} . In contrast, the RVs measured in orders that are less strongly affected by telluric contamination, for instance at 0.78 and 0.82 μm in the VIS and the wavelength region between 1.02 and 1.06 μm in the NIR, are consistent.

We then extended our analysis to the entire VIS and NIR sample of GJ 1012 using the spectra before and after the telluric correction and investigated the impact of the correction by considering the difference between the RVs measured in the individual orders and the resulting median RV values. Our results are presented in Fig. 7c for the VIS channel and in Fig. 8c for the NIR channel. The behavior is similar to that in the case of a single observation. In particular, we found that our correction strongly affects those orders that are most heavily contaminated with telluric features. The inspection of the whole sample confirms that the telluric correction does not yield an improvement in the RV precision in the orders around 0.56–0.62 μm .

We show the VIS and NIR RV time series derived before and after telluric correction in Fig. 9. To account for systematic instrumental drifts, we corrected the RVs for nightly zero-point offsets, which were obtained from a sample of RV-quiet stars with RV variations smaller than 10 m s^{-1} observed in the same night (Trifonov et al. 2018; Tal-Or et al. 2019). In the VIS channel, we determined a weighted rms of 2.2 m s^{-1} using RVs measured from uncorrected spectra and 2.3 m s^{-1} for those measured from corrected spectra. The slight increase of the rms value can be mainly explained by the larger RV dispersion of the bluest VIS orders. In the heavily contaminated red orders of the VIS arm the RV scatter is decreased by several hundreds m s^{-1} , which leads to a consistent set of RVs also in these orders. Over the entire VIS arm, this gain is nearly counterbalanced by additional RV scatter in the wavelength range below 0.62 μm , which we attribute to the telluric correction. In the case of the NIR channel, the rms was considerably reduced from 9.5 m s^{-1} for the RVs derived from the uncorrected spectra to 5.7 m s^{-1} for those derived after the correction. Our results are listed in Table 4.

The lower limit of achievable RV precision is defined by the internal RV precision σ_{int} and depends on the S/N of each observation and the spectral information content (Quirrenbach et al.

Table 4. Weighted rms and median internal precisions $\tilde{\sigma}_{\text{int}}$ derived from VIS and NIR RVs of GJ 1012 before and after telluric correction.

	Before		After	
	VIS	NIR	VIS	NIR
rms [m/s]	2.2	9.5	2.3	5.7
$\tilde{\sigma}_{\text{int}}$ [m/s]	1.6	6.3	1.5	4.6

2018). By including spectral ranges that were masked before the telluric correction, the usable amount of the stellar spectrum and therefore the spectral information content is increased, thus, resulting in a reduction of σ_{int} in both channels after the correction. The improvement in the VIS channel is rather moderate, where the median internal RV precision $\tilde{\sigma}_{\text{int}}$ drops down from 1.6 m s^{-1} before the correction to 1.5 m s^{-1} afterwards. In the NIR channel, however, we obtain a substantial enhancement where $\tilde{\sigma}_{\text{int}}$ falls from 6.3 m s^{-1} before the correction to 4.6 m s^{-1} after the correction. Again, we provide our findings in Table 4. Our results in the near-infrared demonstrate that telluric contaminated wavelength regions carry a significant amount of RV information, which is accessible after the correction. In fact, the rms in the NIR channel after the correction is 5.7 m s^{-1} and therefore below the internal precision limit of 6.3 m s^{-1} before the correction. The use of a less conservative mask, for instance a 40 % mask, is expected to engender an even larger improvement of σ_{int} .

5. Summary and conclusions

We have presented the TDTM technique, a combination of data-driven (template construction) and forward-modeling (spectral fitting) methods to correct for telluric absorption lines in high-resolution optical and near-infrared spectra. After applying a telluric mask to a time series of spectra, we construct a high S/N stellar template, and use it to remove the stellar contribution from the observations. We then use `molecfit` to fit an atmospheric transmission model to the resulting telluric spectrum and finally correct the target spectrum at all wavelengths. While the telluric correction via spectral modeling with `molecfit` alone is especially challenging for late type stars with their high density of molecular lines, the TDTM technique is applicable to spectra of any spectral type. Although we chose the `molecfit` code to fit the transmission model to the telluric spectra in this work, other software packages that produce synthetic atmospheric transmission spectra, such as the TelFit⁹ (Gullikson et al. 2014) or TAPAS¹⁰ code (Bertaux et al. 2014), could be used.

Telluric correction with our method works best with a high number of observations and good coverage of the barycentric velocity space. To demonstrate the performance of our correction method we applied it to high-resolution optical and near-infrared CARMENES observations of 109 Vir and GJ 273. We found that `molecfit` corrects telluric lines with a depth of up to $\sim 50\%$ close to the noise level in the residual telluric transmission spectrum obtained with the help of the template.

We investigated the impact of telluric features and our correction on high-precision RVs using real data and present the improvement in RV that can be achieved in the optical and the near-infrared wavelength range. After we applied our telluric correction approach to a time series of 22 VIS and 13 NIR spectra of

the RV-quiet M4.0 V star GJ 1012 obtained with CARMENES, we determined the RVs using a 30 % telluric mask and compared them to the RVs derived with the standard RV pipeline SERVAL, which employs a telluric masking with a 5 % mask. By exploring the RV signals in the different spectral orders, we find that the largest impact can be attributed to the most severely affected orders adjacent to the strong water bands at 0.82, 0.95, 1.14, and $1.40 \mu\text{m}$.

Despite improvement in the red part of the VIS arm, no significant improvement in RV precision was obtained considering the entire VIS arm of CARMENES. In fact, a slight increase of the rms from 2.2 m s^{-1} for the uncorrected spectra compared to an rms of 2.3 m s^{-1} for the corrected spectra was found. This indicates that a telluric binary mask is sufficient in the case of objects with a large RV information content at optical wavelengths. However, for observations at high airmass and objects with fewer spectral features such as Sun-like stars, a comprehensive treatment of the telluric lines may still be necessary (Luque et al. 2019).

In the near-infrared wavelength range, we find that telluric contamination is strongly alleviated by the TDTM technique and, thus, the usable fraction of the spectrum increases. An improved telluric correction in the near-infrared is relevant for spectral analysis and of course the measurement of RVs. Our telluric correction decreases the RV scatter and improves the rms from 9.5 m s^{-1} for uncorrected spectra, where features deeper than 5 % are simply masked, to 5.7 m s^{-1} for telluric corrected spectra.

As a consequence of the increase of the usable stellar spectrum, the examination of the median internal RV precision revealed a moderate enhancement from 1.6 to 1.5 m s^{-1} in the VIS channel and a considerable improvement from 6.3 to 4.7 m s^{-1} in the NIR channel. With our approach, we made the stellar information content in regions with moderate telluric contamination accessible and used it to improve the RV precision. Our results highlight the importance of a proper telluric line treatment in the analysis of near-infrared spectra and the determination of RVs. The improvement in near-infrared RV precision enables us to search for Earth-like planets around M dwarfs more efficiently, in particular, the those very late-type M dwarfs, which are too faint in the VIS arm regime.

Acknowledgements. CARMENES is an instrument for the Centro Astronómico Hispano-Alemán de Calar Alto (CAHA, Almería, Spain). CARMENES is funded by the German Max-Planck-Gesellschaft (MPG), the Spanish Consejo Superior de Investigaciones Científicas (CSIC), the European Union through FEDER/ERF FICTS-2011-02 funds, and the members of the CARMENES Consortium (Max-Planck-Institut für Astronomie, Instituto de Astrofísica de Andalucía, Landessternwarte Königstuhl, Institut de Ciències de l’Espai, Institut für Astrophysik Göttingen, Universidad Complutense de Madrid, Thüringer Landessternwarte Tautenburg, Instituto de Astrofísica de Canarias, Hamburger Sternwarte, Centro de Astrobiología y Centro Astronómico Hispano-Alemán), with additional contributions by the Spanish Ministry of Economy, the German Science Foundation through the Major Research Instrumentation Programme and DFG Research Unit FOR2544 “Blue Planets around Red Stars”, the Klaus Tschira Stiftung, the states of Baden-Württemberg and Niedersachsen, and by the Junta de Andalucía. Based on data from the CARMENES data archive at CAB (INTA-CSIC). We acknowledge financial support from the Agencia Estatal de Investigación del Ministerio de Ciencia, Innovación y Universidades and the European FEDER/ERF funds through projects AYA2016-79425-C3-1/2/3-P, AYA2015-69350-C3-2-P, and the Centre of Excellence “Severo Ochoa” and “María de Maeztu” awards to the Instituto de Astrofísica de Canarias (SEV-2015-0548), Instituto de Astrofísica de Andalucía (SEV-2017-0709), and Centro de Astrobiología (MDM-2017-0737), and the Generalitat de Catalunya/CERCA programme. L.T.-O. acknowledges support from the Israel Science Foundation (grant No. 848/16).

⁹ <https://pypi.org/project/TelFit/>

¹⁰ Transmissions Atmosphériques Personnalisées pour l’Astronomie, <http://cds-espri.ipsl.fr/tapas/>

References

- Anglada-Escudé, G. & Butler, R. P. 2012, ApJS, 200, 15
- Artigau, É., Astudillo-Defru, N., Delfosse, X., et al. 2014, in Proc. SPIE, Vol. 9149, Observatory Operations: Strategies, Processes, and Systems V, 914905
- Bailey, J., Simpson, A., & Crisp, D. 2007, PASP, 119, 228
- Bedell, M., Hogg, D. W., Foreman-Mackey, D., Montet, B. T., & Luger, R. 2019, arXiv e-prints [arXiv:1901.00503]
- Bertaux, J. L., Lallement, R., Ferron, S., Boonne, C., & Bodichon, R. 2014, A&A, 564, A46
- Caballero, J. A., Guàrdia, J., López del Fresno, M., et al. 2016, SPIE, 9910, 0E
- Caccin, B., Cavallini, F., Ceppatelli, G., Righini, A., & Sambuco, A. M. 1985, A&A, 149, 357
- Clough, S. A., Shephard, M. W., Mlawer, E. J., et al. 2005, J. Quant. Spec. Radiat. Transf., 91, 233
- Cutri, R. M., Skrutskie, M. F., van Dyk, S., et al. 2003, VizieR Online Data Catalog, II/246
- Donati, J.-F., Kouach, D., Lacombe, M., et al. 2018, SPIRou: A NIR Spectropolarimeter/High-Precision Velocimeter for the CFHT, 107
- Gaia Collaboration, Brown, A. G. A., Vallenari, A., et al. 2018, A&A, 616, A1
- García-Piquer, A., Morales, J. C., Ribas, I., et al. 2017, A&A, 604, A87
- Gordon, I. E., Rothman, L. S., & Toon, G. C. 2011, Journal of Quantitative Spectroscopy and Radiative Transfer, 112, 2310
- Gullikson, K., Dodson-Robinson, S., & Kraus, A. 2014, AJ, 148, 53
- Halverson, S., Terrien, R., Mahadevan, S., et al. 2016, in Proc. SPIE, Vol. 9908, Ground-based and Airborne Instrumentation for Astronomy VI, 99086P
- Husser, T.-O. & Ulbrich, K. 2014, in Astronomical Society of India Conference Series, Vol. 11, Astronomical Society of India Conference Series
- Husser, T.-O., Wende-von Berg, S., Dreizler, S., et al. 2013, A&A, 553, A6
- Kausch, W., Noll, S., Smette, A., et al. 2015, A&A, 576, A78
- Kotani, T., Tamura, M., Nishikawa, J., et al. 2018, SPIE, 10702, 11
- Kürster, M., Endl, M., Rouesnel, F., et al. 2003, A&A, 403, 1077
- Lockwood, A. C., Johnson, J. A., Bender, C. F., et al. 2014, ApJ, 783, L29
- Luque, R., Nowak, G., Pallé, E., et al. 2019, A&A, 623, A114
- Mahadevan, S., Ramsey, L. W., Terrien, R., et al. 2014, in Proc. SPIE, Vol. 9147, Ground-based and Airborne Instrumentation for Astronomy V, 91471G
- Quirrenbach, A., Amado, P. J., Ribas, I., et al. 2018, SPIE, 10702, 0W
- Reiners, A., Zechmeister, M., Caballero, J. A., et al. 2018, A&A, 612, A49
- Rothman, L. S., Gordon, I. E., Barbe, A., et al. 2009, J. Quant. Spec. Radiat. Transf., 110, 533
- Royer, F., Zorec, J., & Gómez, A. E. 2007, A&A, 463, 671
- Rudolf, N., Günther, H. M., Schneider, P. C., & Schmitt, J. H. M. M. 2016, A&A, 585, A113
- Sameshima, H., Matsunaga, N., Kobayashi, N., et al. 2018, PASP, 130, 074502
- Seifahrt, A., Käuf, H. U., Zängl, G., et al. 2010, A&A, 524, A11
- Smette, A., Sana, H., Noll, S., et al. 2015, A&A, 576, A77
- Tal-Or, L., Trifonov, T., Zucker, S., Mazeh, T., & Zechmeister, M. 2019, MNRAS, 484, L8
- Trifonov, T., Kürster, M., Zechmeister, M., et al. 2018, A&A, 609, A117
- Vacca, W. D., Cushing, M. C., & Rayner, J. T. 2003, PASP, 115, 389
- Wildi, F., Blind, N., Reshetov, V., et al. 2017, SPIE, 10400, 18
- Zechmeister, M., Anglada-Escudé, G., & Reiners, A. 2014, A&A, 561, A59
- Zechmeister, M., Kürster, M., & Endl, M. 2009, A&A, 505, 859
- Zechmeister, M., Reiners, A., Amado, P. J., et al. 2018, A&A, 609, A12

Appendix A: Instrumental line profile

For a proper modeling of the telluric lines, the line spread function (LSF) needs to be well known. In order to characterize the LSF, we analyze hollow cathode lamp spectra taken for the purpose of calibration before and after the science observations.

An accurate estimation of the line shape is not trivial, since the lines are sparsely sampled. Within each échelle order, the coverage of the FWHM of the LSF typically increases from around 2.5 to 4 pixels when moving along the main dispersion direction from the blue to the red part of the order. Due to several instrumental effects (e.g. temperature variations), the spectra move across the detector with time. We therefore combined multiple exposures to artificially increase the sampling. In the visual channel 1455 different lamp exposures (2605 in the near-infrared) have been used for this purpose. For each line investigated in that manner (114 in the near-infrared and 218 in the visual) the frames have been aligned so that the line was centered. Before combination they were normalized.

These superimposed line profiles are well suited to model the shape of the LSF. For this purpose we tested different profiles, namely Gaussians and Lorentzians, generalized Gaussians and Lorentzians with the exponent treated as an additional free parameter, as well as Voigt profiles. The analysis of all fits showed that a Voigt profile is most appropriate for the LSF modeling. The other profiles usually were not suitable to handle both the line cores and lobes properly at the same time.

In addition, we investigated the variations in the measured line widths, $\Delta\lambda$, across the detector and found that aside from some secondary, although significant, features near the detector edges (particularly in the blue part of the VIS sensor), the line widths still can be described in a consistent manner. The most dominant effect becomes apparent, when the widths of the lines are expressed in terms of wavelength. In the Voigt profile the overall width can be described by its Gaussian and Lorentzian components. Both are expected to show a linear trend in wavelength if the resolution is constant. However, when the entities are expressed in a wavelength independent way choosing units of $\Delta\lambda/\lambda_c$, where λ_c represents the central vacuum wavelength of the particular line, these normalized widths are expected to remain constant, if the resolution of the spectrograph is independent of wavelength. $\Delta\lambda/\lambda_c$, can be directly measured from the widths of unresolved lines.

In Fig. A.1 the measured Gaussian and Lorentzian FWHM components of the Voigt profile are shown for both channels. The NIR channel has a somewhat lower resolution, and therefore wider Gaussian component than the VIS channel. However, the widths of the Lorentzian component are very similar for both channels.

To obtain robust estimates of the LSF parameters, we use medians for the FWHM of each component and channel to model the instrumental line spread function of CARMENES. These parameters are summarized in Table A.1. Due to the clearly visible deviation in the blue part of the visual channel we have considered only lines with a wavelength above 6000 Å. Also, the distribution of the Lorentzian component, particularly in the NIR part of the spectrum, shows some conspicuous features. Some outliers cluster around 12 500 Å, while the scatter seems generally increased for wavelengths above 15 000 Å. The reasons for those effects could not consistently and objectively be traced back to line blends or similar effects.

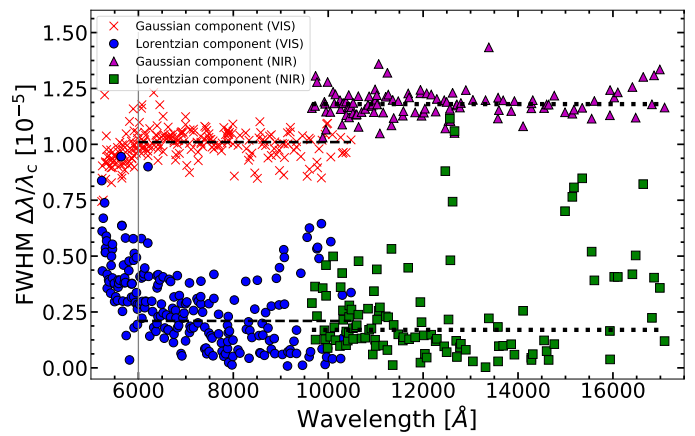


Fig. A.1. Measured Gaussian and Lorentzian FWHM components of Hollow cathode emission lines as a function of wavelength for the optical (VIS) and near-infrared (NIR) CARMENES spectrographs. The gray vertical line marks the cut-off wavelength at 6000 Å. The horizontal lines indicate median values of the Gaussian and Lorentzian FWHM components for the optical channel (dashed lines) and the near-infrared channel (dotted lines).

Table A.1. Median averaged Gaussian and Lorentzian FWHM.

Channel	#lines	$w_{\text{Gauss}} [\Delta\lambda/\lambda_c]$	$w_{\text{Lorentz}} [\Delta\lambda/\lambda_c]$
VIS	218	1.00×10^{-5}	2.8×10^{-6}
VIS (> 6000 Å)	159	1.01×10^{-5}	2.1×10^{-6}
NIR	114	1.18×10^{-5}	1.7×10^{-6}

Appendix B: Approximation of the convolution equation

In an actual observation, the product of the stellar spectrum, s , and the telluric transmission spectrum, t , is received by the system of telescope and spectrograph, which we call the instrument. The effect of the instrument on the received spectrum is modeled by a convolution with the instrumental line spread function, L , so that we obtain the left hand side of the equation

$$[s(\lambda) \cdot t(\lambda)] \otimes L(\lambda) \approx [s(\lambda) \otimes L(\lambda)] \cdot [t(\lambda) \otimes L(\lambda)]. \quad (\text{B.1})$$

As the convolution cannot easily be inverted, the left hand side of Eq. (B.1) is frequently approximated as a product of two spectra separately convolved with the line spread function. As previously pointed out, e.g., by Sameshima et al. (2018), the two sides of the equation differ. In their analysis, Sameshima et al. (2018) found that a telluric-corrected spectrum based on this approximation noticeably differs from the stellar spectrum if the width of the stellar lines is comparable to or narrower than the instrumental resolution and if the stellar lines are heavily blended with telluric features.

We analytically investigate the difference between both sides of Eq. (B.1), making the simplifying assumption of normality for the stellar, telluric, and instrumental line profiles. In particular,

we adopt

$$s(\lambda) = \frac{A_s}{\sqrt{2\pi\sigma_s^2}} \exp\left(-\frac{(\lambda - \mu_s)^2}{2\sigma_s^2}\right) \quad (B.2)$$

$$t(\lambda) = A_t N(\mu_t, \sigma_t^2), \quad (B.3)$$

$$L(\lambda) = N(0, \sigma_L^2). \quad (B.4)$$

Substituting $s(\lambda)$, $t(\lambda)$, and $L(\lambda)$ into the left hand side of Eq. (B.1) leads to

$$\begin{aligned} & [s(\lambda) \times t(\lambda)] \otimes L(\lambda) \\ &= \frac{A_s A_t}{2\pi\sigma_z^2} \exp\left(-\frac{(\lambda - \mu_s)^2\sigma_s^2 + (\lambda - \mu_t)^2\sigma_t^2 + (\mu_s - \mu_t)^2\sigma_L^2}{2\sigma_z^4}\right) \quad (B.5) \\ &= a, \end{aligned}$$

where $\sigma_z^4 = \sigma_s^2\sigma_t^2 + \sigma_s^2\sigma_L^2 + \sigma_t^2\sigma_L^2$ and a abbreviates Eq. (B.5). Using

$$s(\lambda) \otimes L(\lambda) = A_s N(\mu_s, \sigma_s^2 + \sigma_L^2) \quad (B.7)$$

$$t(\lambda) \otimes L(\lambda) = A_t N(\mu_t, \sigma_t^2 + \sigma_L^2) \quad (B.8)$$

we find that the substitution of $s(\lambda)$, $t(\lambda)$, and $L(\lambda)$ into the right hand side of Eq. (B.1) leads to

$$\begin{aligned} & [s(\lambda) \otimes L(\lambda)] \cdot [t(\lambda) \otimes L(\lambda)] = \\ & \frac{A_s A_t}{2\pi \sqrt{\sigma_z^4 + \sigma_L^4}} \exp\left(-\frac{(\lambda - \mu_s)^2}{2(\sigma_s^2 + \sigma_L^2)} - \frac{(\lambda - \mu_t)^2}{2(\sigma_t^2 + \sigma_L^2)}\right) = b, \quad (B.9) \end{aligned}$$

where b again abbreviates our findings.

Appendix B.1: Estimating the difference

The details of the differences between the two sides of Eq. (B.1) depend on the summands represented by a and b and, therefore, the parameters $\mu_{s,t}$, $A_{s,t}$, and $\sigma_{s,t,L}$. Naturally, some estimates can be obtained in special cases.

Assuming a perfectly blended stellar and telluric line $\mu_s = \mu_t = \lambda$, we obtain for the difference between Eq. (B.5) and Eq. (B.9)

$$\begin{aligned} a - b &= \frac{A_s A_t}{2\pi\sigma_z^2} \left(1 - \frac{1}{\sqrt{1 + \frac{\sigma_L^4}{\sigma_z^4}}} \right) \\ &= d_s d_t \frac{\sigma_s \sigma_t}{\sigma_z^2} \left(1 - \frac{1}{\sqrt{1 + \frac{\sigma_L^4}{\sigma_z^4}}} \right), \quad (B.10) \end{aligned}$$

where $d_{s,t}$ denote the line depths

$$d_{s,t} = \frac{A_{s,t}}{\sqrt{2\pi\sigma_{s,t}^2}}. \quad (B.11)$$

In general $\sigma_z^2 \geq \sigma_s \sigma_t$, and we find $a - b \geq 0$ from which follows that $a - b < d_s d_t \frac{\sigma_s \sigma_t}{\sigma_z^2}$. Under the stated assumptions, we therefore find that the accuracy of the approximation depends on the product of the line depths, a fact that also follows from the linearity of the convolution operator in Eq. (B.1).

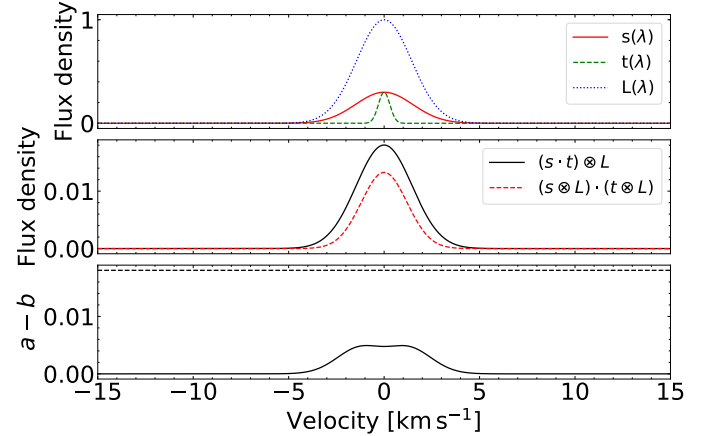


Fig. B.1. Approximation of the convolution function for the special case where a stellar line is blended by a telluric line ($\mu_s = \mu_t$). *Upper panel:* Artificial line profiles representing a stellar line (red line), a telluric line (green dashed), and the instrumental line profile (blue dotted, normalized for the sake of clarity). *Middle panel:* Left and right side of Eq. (B.1). *Lower panel:* Difference between the left and right side of Eq. (B.1) expressed by $a - b$. The dashed line indicates the limit set by the product of the line depths $d_s d_t \frac{\sigma_s \sigma_t}{\sigma_z^2}$.

In Fig. B.1, we illustrate the differences between the two sides of Eq. (B.1) for the special case of a central blend of a stellar and a telluric line (i.e., $\mu_s = \mu_t$) for parameters appropriate for the CARMENES spectrograph. In our approximation, we consider only normal line profiles. We choose the standard deviation of the instrumental line profile, σ_L , such that its FWHM matches that of the true VIS channel Voigt line profile of CARMENES (Table A.1), which yields $\sigma_L = 0.048 \text{ \AA}$. We assumed stellar and telluric lines located at $\mu_s = \mu_t = 10000 \text{ \AA}$ with line depths of $d_s = 0.3$ and $d_t = 0.3$. The intrinsic stellar and telluric line widths (before convolution by the Instrumental line spread function) were estimated from a synthetic PHOENIX spectrum (Husser et al. 2013) and a telluric transmission model, which yields $\sigma_s = 0.05 \text{ \AA}$ and $\sigma_t = 0.01 \text{ \AA}$. We present the resulting Gaussian profiles in the upper panel of Fig. B.1, the left and right side of Eq. (B.1) in the middle panel of Fig. B.1, and the difference $a - b$ as well as the limit expressed by $d_s d_t \frac{\sigma_s \sigma_t}{\sigma_z^2}$ in the lower panel of Fig. B.1. For the adopted parameters, the difference between the left and right side of Eq. (B.1) is approximately 0.5 %. This is in the range of 2 % cited as the correction accuracy of `molecfit`. For less deep lines, the effect is less pronounced. In the extreme case of very high instrument resolution represented by the limit $\sigma_L \rightarrow 0$, we find that σ_z^2 approaches $\sigma_g \sigma_h$ so that Eq. (B.10) approaches zero and the difference vanishes.

Our results allow to obtain an estimate of the accuracy of the approximation in Eq. (B.1) based on a normal approximation of the line profiles. They are also consistent with the findings of Sameshima et al. (2018).

Appendix C: Additional plots

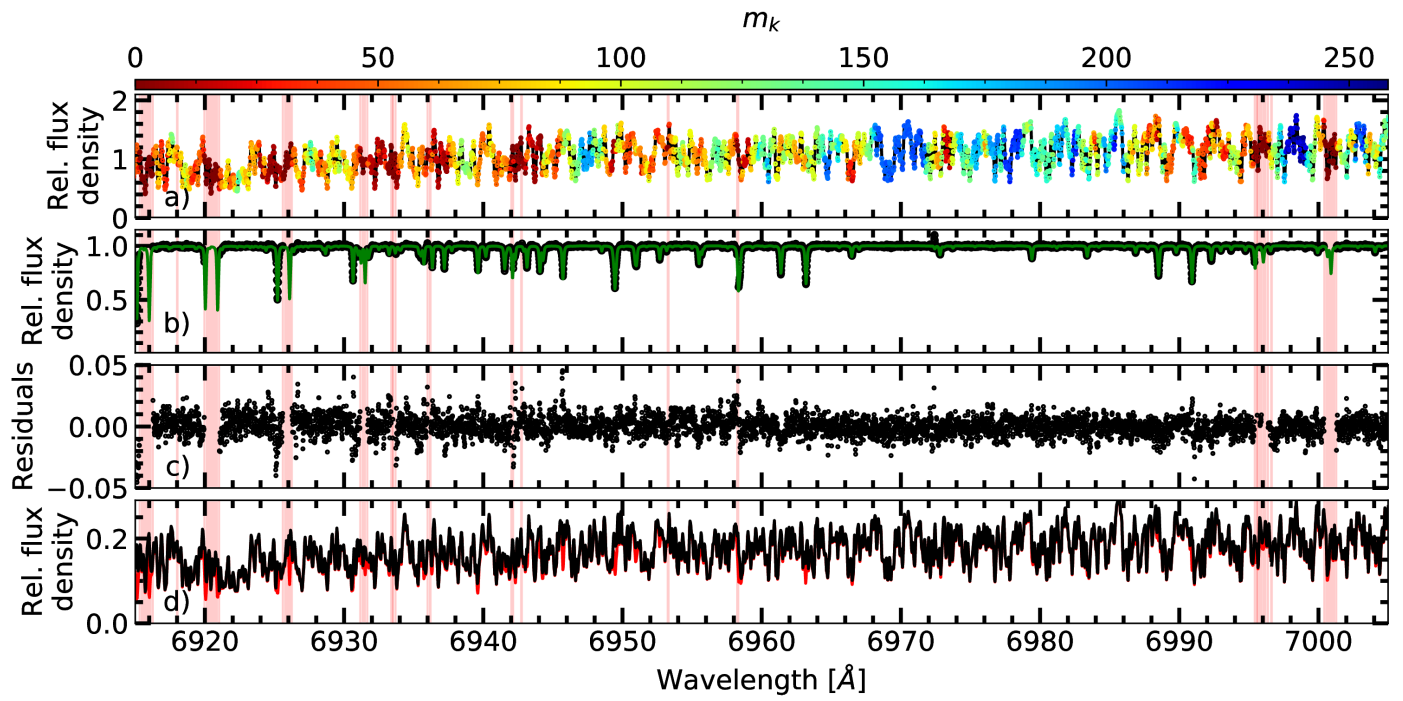


Fig. C.1. Same as Fig. 2 but for O₂ and H₂O features.

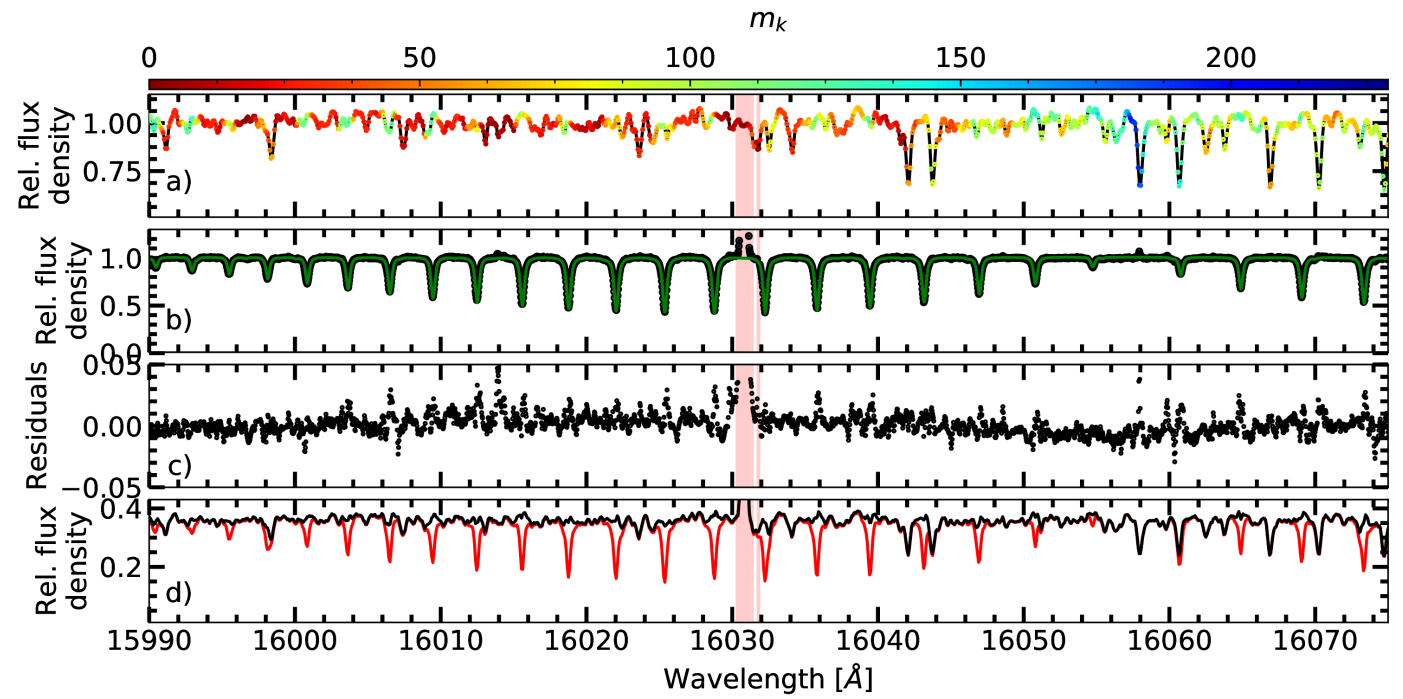


Fig. C.2. Same as Fig. 2 but for the NIR wavelength range, which contains telluric CO₂ features. In addition to template pixels with $m_k = 0$, we also masked telluric emission features.